



1 Spectrometric measurements of atmospheric propane (C_3H_8)

2 Geoffrey C. Toon¹, Jean-Francois L. Blavier¹, Keeyoon Sung¹, Katelyn Yu^{1,2}

3 ¹ Jet Propulsion Laboratory, California Institute of Technology, Pasadena, CA, 91109, USA

4 ² Dept. Civil and Environmental Engineering, UC Berkeley, Berkeley, CA, 94720, USA

5 *Correspondence to:* Geoffrey.C.Toon@jpl.nasa.gov

6 **Abstract.** We report measurements of atmospheric C_3H_8 from analysis of ground-based, solar absorption spectra
7 from the JPL MkIV interferometer. Using the strong Q-branch absorption feature at 2967 cm^{-1} , we can measure
8 C_3H_8 in locations where its abundance is enhanced by proximity to sources (e.g., large natural gas fields, mega-
9 cities). A case study of MkIV C_3H_8 measurements from Ft. Sumner, New Mexico, show large variations that are
10 strongly correlated with ethane (C_2H_6) amounts and with back-trajectories from SE New Mexico and West Texas,
11 where the Permian Basin oil and natural gas field is located. Measurements from JPL, California, also show large
12 C_3H_8 enhancements on certain days, but more correlated with CO than C_2H_6 . From MkIV solar occultation
13 measurements from balloon, C_3H_8 was not detected at any altitude in any flight.

14 1. Introduction

15 Non-methane hydrocarbons such as C_3H_8 and C_2H_6 affect air quality because their oxidation enhances tropospheric
16 O_3 and aerosol pollution. They are also sensitive indicators of fugitive losses by the oil and natural gas industry, an
17 important source of co-emitted methane (CH_4), a greenhouse gas. These fugitive losses appear to be under-
18 estimated in global inventories (Dalsoren et al., 2018).

19 Atmospheric C_3H_8 and C_2H_6 are entirely the result of emissions at the surface. In pre-industrial times these came
20 from geological seeps and wild fires, but in recent times these natural sources have been surpassed by emissions
21 from fossil fuel production. The latter peaked in about 1970, and then declined due to stricter regulation of
22 emissions from the oil and natural gas industry and automobiles. But in the past decade, this decreasing trend has
23 reversed due to accelerated NG exploitation (Helmig et al., 2016).

24 C_3H_8 has a lifetime of about 2 weeks in summer and 8 weeks in winter (Rosado-Reyes et al., 2007). This is mostly
25 dictated by how fast it is being oxidized by reactions with hydroxyl radicals and chlorine atoms. In contrast, the
26 lifetime of C_2H_6 is 2–6 months, which is 3–4 times longer than that of C_3H_8 . Given this 2–8 week lifetime, a single
27 strong source of propane has the potential to degrade air quality over most of the hemisphere.

28 Unprocessed, in-the-ground, “wet” natural gas is usually between 70–95% CH_4 , 1–15% C_2H_6 , 1–10% C_3H_8 , and 0–
29 3% C_4H_{10} . The latter two gases are typically extracted to form Liquefied Petroleum Gas (LPG). In the northern
30 hemisphere winter, LPG contains more C_3H_8 , while in summer it contains more butane (C_4H_{10}), reducing variations
31 in its vapor pressure.



32 LPG burns much more cleanly than fuel oil and is therefore is increasingly used for heating, and cooking, especially
33 in rural areas that are not served by piped NG. LPG is also used to fuel commercial vehicles, and is increasingly
34 replacing CFCs as a refrigerant and as an aerosol propellant. As a result of extracting LPG from natural gas, the NG
35 that is piped to our homes in urban areas is highly depleted in C_3H_8 and C_4H_{10} , as compared with wet NG.

36 To the best of our knowledge, there are no previous remote sensing measurements of C_3H_8 , although in situ
37 measurements exist. Dalsoren et al. (2018) report surface in situ C_3H_8 amounts of essentially zero at Zeppelin station
38 in Svalbad in summer 2011, but with values of 1 ppb in the winter, with peaks of up to 2.4 ppb. These C_3H_8 peaks
39 are strongly correlated with C_2H_6 which reaches 3.4 ppb. Using in situ C_3H_8 data from multiple sites Helmig et al.
40 (2016) show large a seasonal cycle in surface in situ C_3H_8 at high NH latitudes, reaching 1 ppb in winter, with little
41 in the SH. They also show increasing C_3H_8 over central and Eastern US over the period 2009.5–2014.5, but no
42 increase on the West coast.

43 Since C_3H_8 correlates with C_2H_6 , both having NG as their main source, we also consider the previous measurements
44 of C_2H_6 . Angelbratt et al. (2011) reported a 0–2%/year decline over the period 1996 to 2006 based on data from six
45 NH FTIR sites. Franco et al (2015) reported a shallow minimum in C_2H_6 in the 2005–2010 based on ground-based
46 FTIR solar spectra above the Jungfraujoch scientific station. Helmig et al. (2016) report a minimum in atmospheric
47 C_2H_6 in 2005–2010 based on in situ and remote measurements.

48 Franco et al. (2016) estimate a 75% increase in North American C_2H_6 emissions between 2008 and 2014, and as a
49 result report a 3–5% annual increase in column C_2H_6 at Northern mid latitudes. They hypothesize that this increase
50 is the result of the recent massive growth in the exploitation of shale gas and tight oil reservoirs in North America,
51 where the drilling productivity began to grow rapidly after 2009.

52 **2. Methods**

53 **2.1 MkIV Instrument**

54 The JPL MKIV interferometer (Toon, 1991) is a high-resolution FITR spectrometer built at JPL in 1984. It covers
55 the entire $650\text{--}5650\text{ cm}^{-1}$ simultaneously in every spectrum with two detectors: a HgCdTe photoconductor covering
56 $650\text{--}1800\text{ cm}^{-1}$ and an InSb photodiode covering $1800\text{--}5650\text{ cm}^{-1}$. For ground-based observations a maximum OPD
57 of 117 cm is employed providing a spectral resolution of 0.005 cm^{-1} . The MKIV is primarily a balloon instrument
58 and has performed 25 flights since 1989, the latest in 2019. Between balloon flights it makes ground-based
59 observations. Since 1985 it has taken 5000 ground-based observations on 1200 different days from 12 different
60 sites. For more detail, see tables in: <https://mark4sun.jpl.nasa.gov/ground.html>

61 **2.2 Retrieval**

62 The analysis of the MKIV spectra was performed with the GFIT (Gas Fitting) tool, a nonlinear, least-squares,
63 spectral-fitting, algorithm developed at JPL. GFIT has been previously used for the Version 3 analysis (Irion et al.,



64 2003) of spectra measured by the Atmospheric Trace Molecule Occultation Spectrometer, and it is currently used for
65 analysis of Total Carbon Column Observing Network spectra (Wunch et al., 2011) and for MkIV spectra (Toon,
66 2016; 2018a; 2018b).

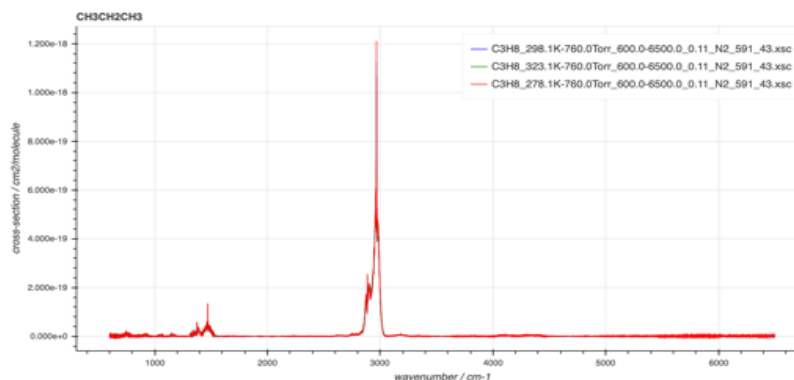
67 GFIT scales the atmospheric gas volume mixing ratio (VMR) profiles to fit calculated spectra to those measured.
68 For C_3H_8 , a 5.4 cm^{-1} -wide fitting window centered on the Q-branch at 2967 cm^{-1} was used. The atmosphere was
69 discretized into 70 layers of 1 km thickness. C_3H_8 and four interfering gases (H_2O , CH_4 , C_2H_6 , HDO) were adjusted.
70 Two frequency stretches were retrieved (telluric and solar). The spectral continuum was fitted as a straight line, and
71 a zero-level offset was fitted. So that's a total of 10 simultaneously-fitted scalars. In addition, the solar pseudo-
72 transmittance was computed (but not adjusted).

73 The assumed temperature, pressure and H_2O profiles were based on the NCEP 6-hourly analyses for solar noon of
74 each day. The a priori vmr profiles were based on NH mid-latitude profiles. This is exactly the same scheme as used
75 by the GGG2014 TCCON analysis (Wunch et al., 2015), but here we apply it to the MIR MkIV spectra rather than
76 the SWIR TCCON spectra.

77 To estimate the sensitivity of the retrieved C_3H_8 to uncertainties in the assumed a priori profiles of T/P and
78 interfering gases (especially H_2O , CH_4), we retrieve the post-2000 C_3H_8 a second time: using GGG2020 instead of
79 GGG2014. The results, shown in appendix A, show that this changes the retrieved C_3H_8 by less than 10% rms with a
80 bias of only 1.1%.

81 2.3. Spectroscopy

82 It is clear from the infra-red lab spectrum of C_3H_8 (Fig.1), that the feature at 2967 cm^{-1} , caused by various CH_2 and
83 CH_3 stretch vibrational modes, is by far the strongest in the entire infrared. So for solar occultation spectrometry,
84 this is by far the best choice. For thermal emission spectrometry from cold planets such as Titan, on the other hand,
85 then the much weaker CH_3 deform bands around 1400 cm^{-1} would be better (Sung et al., 2013).



86

87 **Figure 1.** Infrared laboratory spectra of C_3H_8 absorption cross-section at 323, 298, and 278K (from hitran.org).



88 An empirical pseudo-line-list (EPLL) of C_3H_8 covering 2560–3280 cm^{-1} was derived from the laboratory cross-
89 sections of Harrison and Bernath (2010). This is described in the unpublished report:

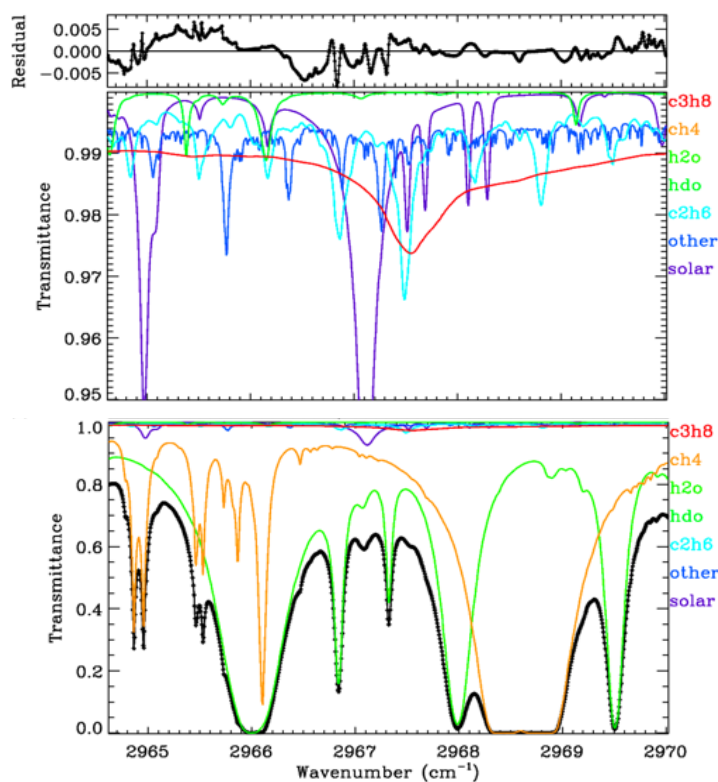
90 https://mark4sun.jpl.nasa.gov/data/spec/Pseudo/c3h8_pll_2560_3280.pdf

91 The use of an EPLL facilitates interpolation and extrapolation of the lab cross-sections to T/P conditions that were
92 not measured in the lab. The fitting of the EPLL also checks the self-consistency of the lab cross-section spectra,
93 and provides an opportunity to correct for artifacts in the lab spectra (e.g. channeling, zero-level offsets,
94 contamination, ILS), although it must be stated that in this particular case the C_3H_8 lab spectra were of very high
95 quality and comprehensive in terms of their coverage. For the interfering C_2H_6 , an EPLL developed eight years ago
96 was used, based on lab measurements of Harrison et al. (2010), as described in the report:

97 https://mark4sun.jpl.nasa.gov/report/C2H6_spectroscopy_evaluation_2850-3050_cm-1.compressed.pdf

98 For other gases the atm.161 linelist was used, which is based on HITRAN 2016, with some empirical adjustments
99 based on fits to lab spectra, especially for H_2O and CH_4 . This is basically the same linelists (atm.161, pll.101) that
100 are used by TCCON, but here we use them in the MIR rather than the SWIR.

101 Figure 2 shows an average spectral fit to the C_3H_8 window in ground-based MkIV spectra, obtained by fitting
102 individual spectra and then averaging the results. The lower panel provides the full transmittance y-range from 0 to
103 1. It can be seen that the main absorbers are CH_4 (orange) and H_2O (green). The C_3H_8 absorption (red) is difficult to
104 discern because it is so shallow. The middle panel shows the same spectral fit, but with the y-scale zoomed into
105 0.95–1.00 transmittance, allowing the weak absorbers like C_3H_8 and C_2H_6 to be more easily seen. The “other”
106 contributions (e.g. O_3) were included in the calculation but not adjusted. The C_3H_8 absorption is fairly flat at about
107 1% depth, except for the Q-branch where it deepens to 2½%. Although the strongest C_2H_6 feature coincides with the
108 C_3H_8 Q-branch, the former is much narrower and there are several additional C_2H_6 features in this window, so we
109 expect little spectrometric “cross-talk” between these two gases. The top panel shows the residuals (measured-
110 calculated transmittance) have some systematic features of ~0.5% in magnitude, especially in the vicinity of the H_2O
111 line at 2966.0 cm^{-1} . Considering the weakness (and smoothness) of the C_3H_8 Q-branch in comparison with the
112 residuals and the contributions of the other gases, we were at first skeptical that a useful C_3H_8 column measurement
113 could be extracted from such spectral fits. But since the analysis of the MkIV spectra is highly automated, it took
114 only a few hours to run the C_3H_8 window shown in Fig.2 over the 5000 MkIV ground-based spectra.



115

116

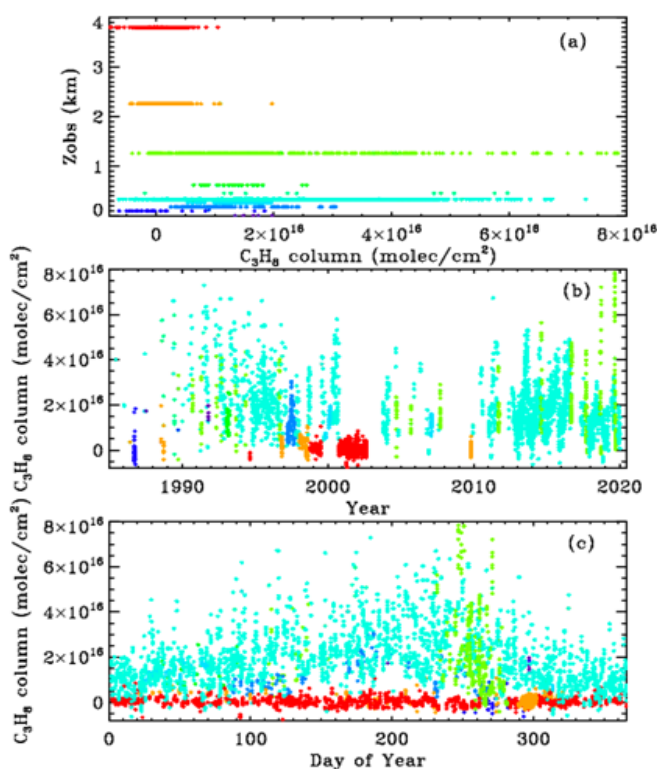
117 **Figure 2.** The average of 5000 ground-based MkIV spectral fits. Black diamonds represent measured spectrum.
118 Black line the fitted calculation. Colored lines represent the contributions of different gases. Bottom panel shows the
119 full transmittance range. Middle panel zooms into the 0.95–1.00 range to help see the weak absorbers (C₂H₆, HDO,
120 and the solar lines). Top panel show residuals (Measured-Calculated); these are generally below 0.5%.

121 3. Results

122 Fig. 3 shows MkIV ground-based C₃H₈ columns, color coded by site altitude. The data were filtered: only points
123 with uncertainties < 1.5E+16 were plotted, reducing the number of plotted points from 5000 to 4700. The top panel
124 (a) shows that at the high-altitude sites (Mt. Barcroft at 3.8 km = Red; Table Mountain Facility at 2.2 km = Orange)
125 the retrieved C₃H₈ columns are centered around zero. Also, the data acquired in Sep 1986 from 0.1 km in Antarctica
126 (dark blue) are also centered around zero. Data acquired from Ft. Sumner, NM, at 1.2 km (lime) have large
127 variations, from zero to nearly 8E+16 molecules.cm⁻², as do the data from JPL at 0.35 km (cyan). Other sites with
128 detectable C₃H₈ include Daggett, CA, (0.6km), Esrange, Sweden (0.26km) in the winter, Fairbanks, AK (0.2km),
129 and Mountain View, CA in late 1991. Panels (b) and (c) show the same C₃H₈ columns, but plotted versus year and
130 day. So C₃H₈ has only been measured by MkIV from northern hemisphere sites within the PBL.



131 High C_3H_8 values ($>4 \times 10^{16}$) can occur at any time of year at JPL (cyan) but most commonly in late summer, as is
132 the case for other pollutants, e.g. CO, probably reflecting the meteorology (stagnant conditions in the LA basin in
133 summer with little replacement of polluted air with clean air from outside). Averaging kernels for these C_3H_8
134 measurements are discussed and illustrated in Appendix B. Suffice it to say here that they range from 0.9 to 1.4 and
135 increase with altitude.



136

137 **Figure 3.** *MkIV* C_3H_8 column abundances from all 12 sites, color-coded by site altitude, as illustrated in panel (a):
138 blue=0.0 km; cyan=0.35 km (JPL); lime=1.2 km (Ft. Sumner); orange=2.25 km (TMF); red=3.8 km (Mt. Barcroft).

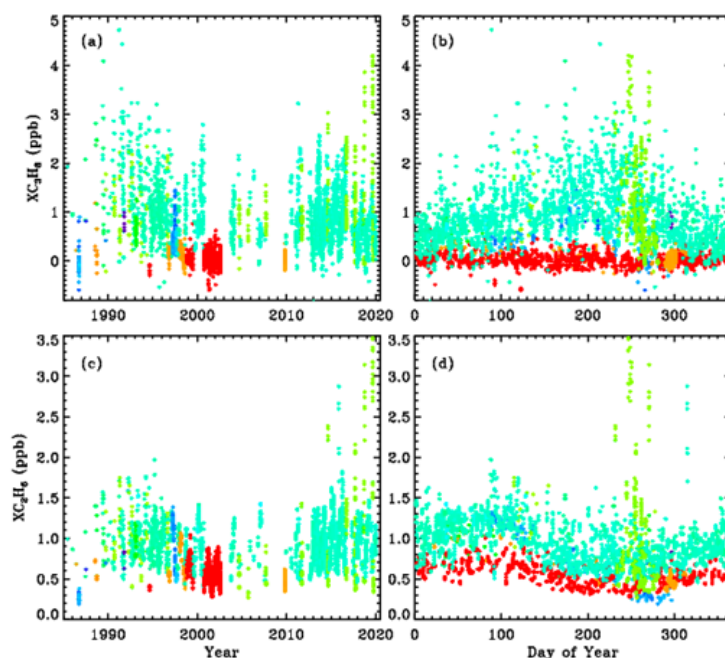
139 The reported uncertainties in our C_3H_8 column measurements are based on the rms fitting residuals compared with
140 the sensitivity of the spectrum to C_3H_8 (Jacobians). At the highest site, Barcroft at 3.8 km ($P=0.65$ atm.), where the
141 interfering H_2O and CH_4 absorptions are relatively weak and narrow, the C_3H_8 column uncertainties are generally
142 smaller than 10^{15} molecules. cm^{-2} . But since the columns themselves are even smaller, no C_3H_8 is detected at
143 Barcroft. At the lower altitude sites such as JPL and Ft. Sumner, the increased interference from H_2O and CH_4 cause
144 the C_3H_8 column uncertainties to be much larger, generally around 5×10^{15} molecules. cm^{-2} at low airmass and
145 worsening rapidly toward higher airmasses. This allows C_3H_8 to be detected at these low-altitude sites under
146 polluted conditions.



147 High C_3H_8 values are also seen at Ft. Sumner, NM (lime), especially in recent years. This was initially a surprise to
148 use because this area has a very low population density, so we naively assumed that we would be measuring
149 background levels of atmospheric pollutants here.

150 We know that the apparent variations in C_3H_8 are real, rather than artifacts, from their strong correlation with C_2H_6 .
151 Figure 4 compares column-averaged C_3H_8 mole fractions (top panels) with those of C_2H_6 (bottom panels). These are
152 the same total C_3H_8 columns shown in Fig.3, but divided by the total column of all gases, which is inferred from the
153 surface pressure. The resulting column-average mole fractions are less sensitive to the site altitudes being different
154 and more easily compared with in situ measurements being in units of mole fraction.

155 The left-hand panels of Fig.4 show the XC_3H_8 time series plotted versus year, and the right-hand panels versus day
156 of the year. The points are color-coded by observation site altitude using the same color scheme as in Fig.3. The data
157 were filtered such that only points with XC_3H_8 uncertainties < 0.74 ppb and C_2H_6 uncertainties < 0.10 ppb were
158 plotted. This reduced the total number of points from 5000 to 4700, so only the best 94% of the data are plotted. It
159 is clear that at JPL (cyan) C_3H_8 has decreased since the 1990s, but that at Ft. Sumner (lime) it has increased over the
160 past decade. The data from these two sites will be explored later.



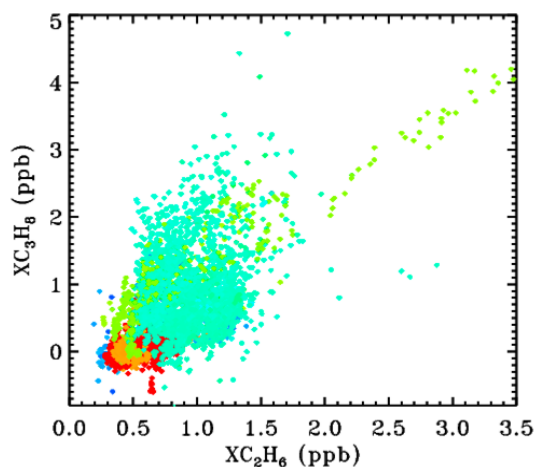
161

162 **Figure 4.** Top panels show measurements of the column-averaged C_3H_8 mole fractions (XC_3H_8). Bottom panels
163 show XC_2H_6 . Left panels show the variation with year. Right-hand panels show the seasonal variation.



164 The lower panels of Fig.4 show XC_2H_6 . This is four times longer-lived than C_3H_8 and never goes to zero because
165 there is always a substantial free tropospheric C_2H_6 component, even in the SH, that varies seasonally: high in
166 spring, low in fall. The Antarctic measurement (blue) are even lower than they appear because days 250 to 300
167 represent the spring in Antarctica, not the fall. The highest ever C_2H_6 was measured from JPL (cyan) in late 2015
168 (day 314) as a result of the Aliso Canyon natural gas leak (Conley et al., 2016). This event is further discussed later
169 and also in Appendix C.

170 Figure 5 shows the XC_2H_6/C_3H_8 correlation plot for all sites. This uses the exact same data, filtering, and color-
171 scheme as for Fig. 4. At JPL (cyan) the correlation is positive but weak. At Ft. Sumner, there are episodes of both
172 gases being enhanced with a strong correlation. In fact, the highest VMRs of C_2H_6 were seen from there, even more
173 than from JPL during the Aliso Canyon gas leak in late 2015.



174

175 **Figure 5.** The correlation between XC_2H_6 and XC_3H_8 for all sites, color-coded by site altitude.

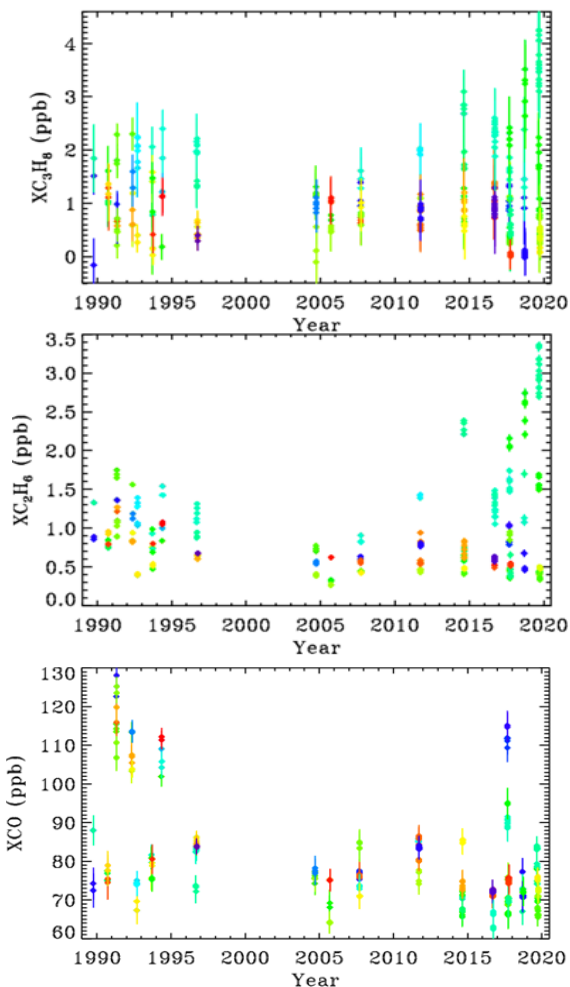
176 3.1. Case Study: Ground-based measurements from Ft. Sumner, NM

177 Ft. Sumner (34.48N, 104.22W, 1.2 km ASL) is the location of the main NASA facility for the launch of
178 stratospheric research balloons. It is located here due to the low population density and hence low risk of mishap.
179 The MkIV instrument has performed balloon campaigns in Ft. Sumner 18 times in the past 30 years. Not all of these
180 campaigns have resulted in a flight, but we have always taken ground-based observations to check that the MkIV
181 instrument is correctly aligned and functional. And to check that telemetry, commanding, and the operation of other
182 experiments do not degrade the MkIV performance.

183 We have taken 520 observations on 106 different days from Ft. Sumner (out of a total of 5000 observations and
184 1200 days). We examine these observations to try to understand whether the large day-to-day C_3H_8 variations are



185 real, and if so, what is causing them. We have already seen a correlation between the XC_3H_8 and XC_2H_6 at all sites
186 in Fig.5, but many points are buried under others, especially at the low values of XC_3H_8 and XC_2H_6 .



187

188

189 **Figure 6.** XC_3H_8 , XC_2H_6 and XCO at Ft. Sumner. MKIV didn't visit Ft. Sumner from 1997 to 2004 because it was
190 performing high-latitude balloon flights from Alaska and Sweden. Since all the observations are made from the
191 same altitude, it no longer makes sense to color code by site altitude. So instead we color-code by mean bearing of
192 the back-trajectory over the previous 36 hours. Dark blue=30°; Light blue=90°, Cyan=120°, Green=180°;
193 Lime=220°; Orange=300°, Red=350°.

194

195 Figure 6 shows that between 1990 and 2005 there was a decrease in C_2H_6 and C_3H_8 measured in Ft. Sumner, by
196 about a factor 2 over 15 years. In recent years (since 2014), however, there has been a large increase in C_2H_6 and

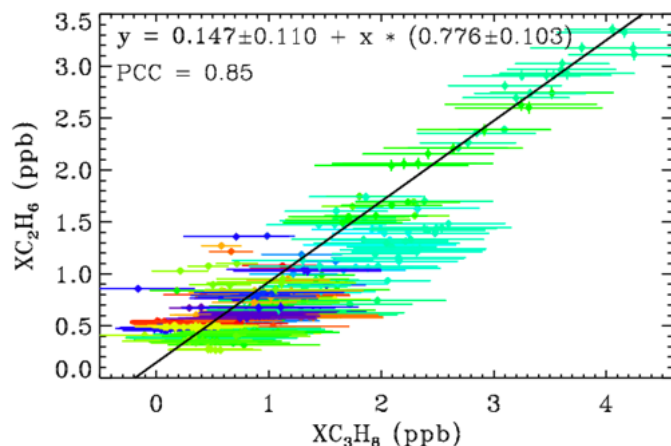


197 C₃H₈ measured at Ft. Sumner, but only when the wind direction is from the SE quadrant (green/lime colors). We see
198 no increase associated with other wind directions (red, blue, orange, yellow).

199 At Ft. Sumner CO has no correlation with wind direction, nor with C₂H₆ or C₃H₈. The majority of days have a
200 column average CO of 75±10 ppb. But there are occasional enhancements up to 120 ppb, likely due to large but
201 distant fires. We do not pursue the CO data any further. They are of no value, other than proving that the C₃H₈
202 sources are different from those of CO.

203 CH₄ is also measured by MkIV. Over the 30-year measurement period XCH₄ has grown from 1650 to 1850 ppb.
204 This secular increase is much larger than any variation due to wind direction. So to be useful, the CH₄ data would
205 have to be detrended, which is not simple given its non-linear growth. Even within the past 4 years, the correlation
206 of XCH₄ with XC₃H₈ was very weak. This is to be expected since the background abundance of CH₄ is more than
207 1000x larger than C₃H₈, whereas wet NG from the Permian Basin is only 6 times richer in CH₄ than C₃H₈. So the
208 NG-induced enhancement of CH₄, as a fraction of its atmospheric background level, will be more than 100 times
209 smaller than that of C₃H₈.

210 Figure 7 shows a XC₃H₈-XC₂H₆ scatter plot using just the Ft. Sumner data. Error bars are much larger for XC₃H₈
211 than for XC₂H₆. This is because the C₂H₆ transitions are stronger and form narrower features, both of which make
212 the retrievals more precise and definitive, whereas most of the C₃H₈ absorption is smeared into a broad continuum
213 which provides little information for this type of retrieval in which the continuum level is fitted. The C₂H₆ features
214 used in the actual C₂H₆ retrieval are at 2976.6 and 2986.6 cm⁻¹ (not shown) and are 3–4 times stronger than those
215 seen in Fig.2.



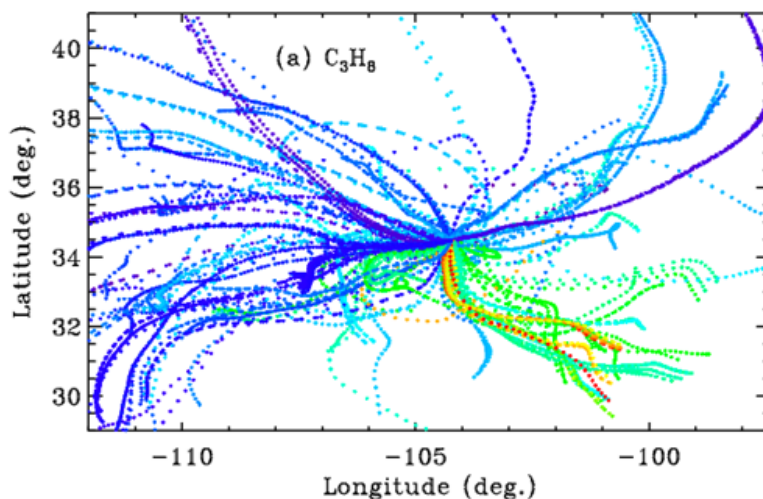
216

217 **Figure 7.** The relationship between XC₃H₈ and XC₂H₆ at Ft. Sumner, color coded for wind direction as for Fig.6.



218 The gradient of the fitted line is 0.78 ± 0.10 implying more C_3H_8 than C_2H_6 . The Pearson Correlation coefficient is
219 0.85, which is high considering the large error bars on the XC_3H_8 . This tight relationship at Ft. Sumner implies that
220 the large variations in the C_3H_8 measurements are not an artifact. Since C_2H_6 can be easily and precisely measured
221 by this technique, it is hard to imagine it being changed by a factor 5 from day to day by an artifact. Much more
222 likely, the common variations in both C_3H_8 and C_2H_6 are real.

223 As already hinted, for each of the 106 observation days from Ft. Sumner we ran hourly HYSPLIT back-trajectories
224 (Stein et al., 2015, Rolph et al., 2017) that bracket the MkIV observation times, then interpolated linearly in time
225 between the two bracketing trajectories. This provided a unique trajectory for each of the 520 observations from Ft.
226 Sumner. The North American Regional Reanalysis (NARR) meteorology was selected which covers North America
227 at 32 km resolution. This is the highest resolution meteorology that covers the entire 1989–2019 observation period.
228 A trajectory altitude of 0.4 km over Ft. Sumner was selected, and these trajectories were extended to 36 hours before
229 the observations in 1-hour steps. Fig.8 shows that the large variations of C_3H_8 are strongly correlated with wind
230 direction. It is very clear that trajectories originating to the SE of Ft. Sumner, carry more C_3H_8 than those from any
231 other direction. A plot was made also for C_2H_6 but not shown due to its strong similarity to Fig.8.



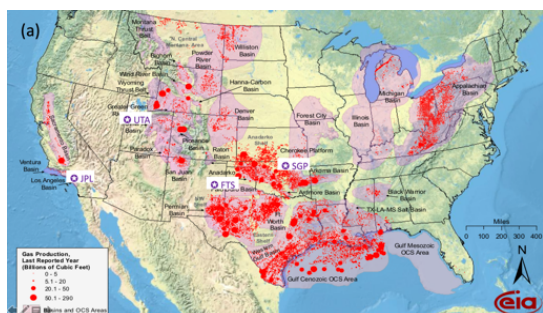
232

233 **Figure 8.** Hourly locations for the back-trajectories, color-coded by XC_3H_8 . Blue=0, Green=2 ppb; Red=4 ppb.
234 Trajectories for which the XC_3H_8 uncertainty exceeded 0.74 ppb are excluded, resulting in only 373 out of 520
235 trajectories being shown. Ft. Sumner lies at 34.2N, 104.2W close to the center of the figure at the confluence of all
236 the back-trajectories. Each point represents a 1-hour time step, so that the wind speed is apparent from the
237 separation of points. Winds from the West are typically stronger than those from the SE quadrant.

238 We also made a scatter plot for CO (not shown) but there was no correlation between CO and wind direction, or
239 between CO and C_3H_8 . This rules out the possibility that the enhanced C_3H_8 and C_2H_6 were somehow associated
240 with distant urban pollution or wild fires.



241 This result leads to speculation on what might be enhancing C_2H_6 and C_3H_8 when the winds come from the SE
242 sector. One of the biggest natural gas production fields in the US lies in the Permian Basin, which underlies the
243 South-East corner of New Mexico and West Texas, as illustrated in Figure 9. This region also includes processing
244 plants where the heavier gases are stripped out of the wet NG, storage facilities for the resulting Natural Gas Liquids
245 (LPG+ethane+pentane), and pipelines. This would suggest that the enhanced C_2H_6 and C_3H_8 is the result of losses
246 from NG production, although this cannot be proven with just one instrument at one site. We would need
247 instruments upwind and downwind to make an accurate assessment of the fluxes.



248
249

250 **Figure 9: (a)** NG production in the lower 48 states of the USA in 2009. Data from the Energy Information
251 Administration: https://www.eia.gov/oil_gas/rpd/conventional_gas.pdf. Superimposed are the locations (purple
252 pentagonal star) of the four sites discussed in detail in this paper: Ft. Sumner in Eastern NM is labelled "FTS". The
253 JPL site in California is labelled "JPL". The locations of the NOAA sites in Utah (UTA) and Oklahoma (SGP) are
254 also included. The Permian basin lies in the SE corner of NM and West Texas.

255 **(b):** [Temporarily removed -- awaiting permission] Illustrating the high number of "liquids-rich" drilling rigs in the
256 Permian Basin, as of Dec. 2019, underscoring its dominance for propane production in the USA. From
257 [https://www.spglobal.com/platts/en/market-insights/latest-news/natural-gas/121919-us-oil-gas-rig-count-rises-for-](https://www.spglobal.com/platts/en/market-insights/latest-news/natural-gas/121919-us-oil-gas-rig-count-rises-for-second-straight-week-everus)
258 [second-straight-week-everus](https://www.spglobal.com/platts/en/market-insights/latest-news/natural-gas/121919-us-oil-gas-rig-count-rises-for-second-straight-week-everus)

259

260 In recent years, the Permian basin has been producing ~15 billion cu.ft. of natural gas (NG) per day
261 (<https://www.eia.gov/petroleum/drilling/pdf/permian.pdf>). A back-of-the-envelope estimate of the contribution of
262 this to the observed C_3H_8 is now performed. We assume that this NG production is distributed over an area that is
263 160 km across. At a wind speed of 20 km/hour, an air mass will take 8 hours to traverse the gas field, during which
264 time $0.72E+19$ molecules. cm^{-2} of NG will have been extracted. Howard et al., (2015), measured the composition of
265 NG from the Permian basin and found that it is very rich in heavy hydrocarbons, being 66.6% CH_4 , 13.7% C_2H_6 and
266 10.3% C_3H_8 by volume. If 4% of this were lost to the atmosphere, and 10.3% of this is C_3H_8 , the total propane
267 column will be enhanced by $3E+16$ molecules. cm^{-2} , which is close to that seen in the highest cases. For C_2H_6 , an
268 enhancement of $4E+16$ would be expected for such a back-trajectory, which is somewhat higher than measured.
269 There will also be an enhancement of CH_4 of about $19E+16$ molec. cm^{-2} , but this represents only 0.5% of the total
270 CH_4 column above Ft. Sumner and will therefore be difficult to discern in the presence of other confounding factors



271 (stratospheric transport, seasonal and longer-term changes). Of course, in cases of higher wind-speeds, or
272 trajectories that partially circumvent the basin, the duration will be less than 8 hours and so the uptake of
273 hydrocarbons will be smaller.

274 A puzzle in our findings is that when both C_3H_8 and C_2H_6 are elevated, we measure more C_3H_8 than C_2H_6 . Yet
275 independent essays of well-head wet NG always find more C_2H_6 than C_3H_8 in the Permian basin (Howard et al.,
276 2015). One possibility is that the C_3H_8 coming from leaking wet NG is augmented by leaks of LPG, stripped from
277 wet NG. This would further enhance the C_3H_8 (and C_4H_{10}) with little C_2H_6 increase.

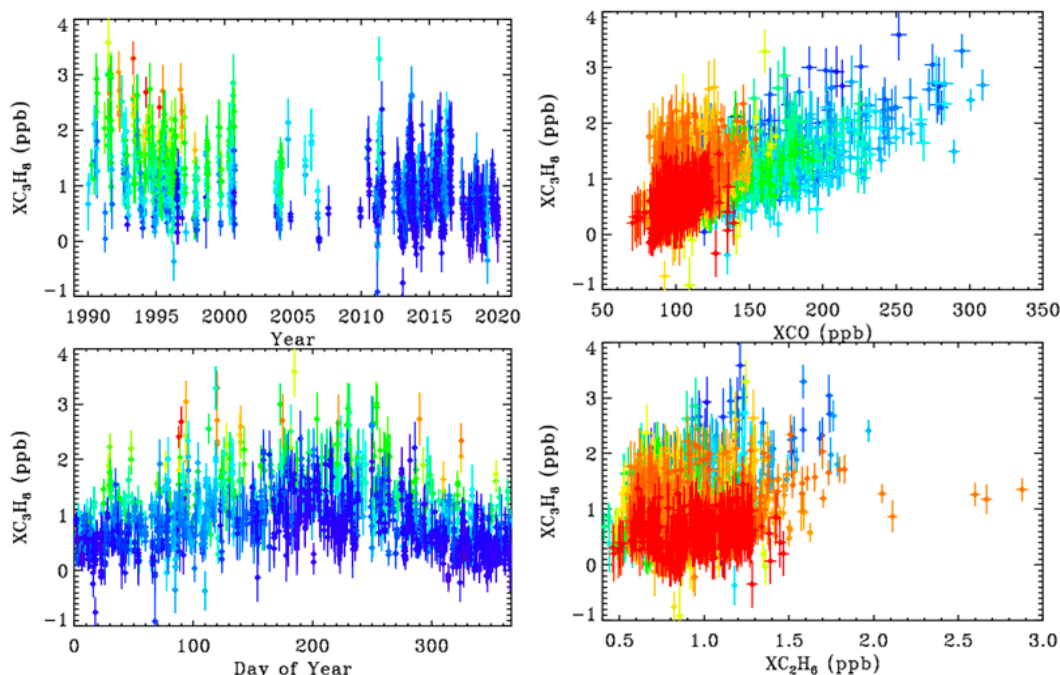
278 We note that the C_2H_6 averaging kernel is 0.7 at the surface versus 0.9 for C_3H_8 (see Appendix B). So when these
279 gases exceed their priors in the PBL, which is likely at high enhancements, both will be under-estimated, but C_2H_6
280 more so than C_3H_8 . So this effect would cause the C_2H_6/C_3H_8 ratio to be 25% low, which explains half the problem,
281 but not all.

282 Alternatively, there could be a systematic over-estimate of the MkIV C_3H_8 due to a mundane multiplicative bias in
283 the C_3H_8 spectroscopy. This would over-estimate all the C_3H_8 measurements without degrading the strong
284 correlation with C_2H_6 , but seems unlikely.

285 3.2. Case Study: Ground-based measurements from JPL

286 The Jet Propulsion Laboratory (34.2N; 118.17W; 0.35 km altitude) lies at the Northern edge of the Los Angeles
287 basin. When winds are from the North (rare in summer) air quality is good. When conditions are stagnant (common
288 in summer) pollutants accumulate and so air quality is poor. C_3H_8 measured at JPL exhibits very different behavior
289 to that at Ft. Sumner. It decreases over time, exhibits little correlation with C_2H_6 , and positive correlation with CO.
290 Figure 10 illustrates these behaviors.

291 The left-hand panels of Fig. 10 shows XC_3H_8 time series measured from JPL, color coded by CO. The upper-left
292 panel shows a large decrease in C_3H_8 from 1–3 ppb in 1990 to less than 1 ppb in 2019. This mirrors the decrease in
293 CO over JPL (not shown) over the same period. The lower-left panel shows a large seasonal component to the
294 C_3H_8 , with a peak in late summer, when the air is most stagnant over JPL allowing pollutants to accumulate. The
295 highest C_3H_8 values appear red or orange (high CO), while the lowest appear blue (low CO), implying an
296 association with CO. This is confirmed in the upper-right panel which plots C_3H_8 directly against CO. The right-
297 hand panels are color-coded by year. The C_3H_8 correlation is mostly a result of both gases having decreased over the
298 30-year record. But even within each year, there still remains a positive correlation. This does not necessarily mean
299 that C_3H_8 and CO have the same source, but that their sources are spatially coincident.



300

301 **Figure 10.** Column-average C_3H_8 above JPL. **Left Panels:** The time series color-coded by CO (red=250 ppb;
302 green= 130 ppb; blue=100 ppb). **Right Panels:** The relationship between XC_3H_8 and CO and C_2H_6 color-coded by
303 year (blue=1990; green=2005; red=2019).

304

305 The lower-right panel shows C_3H_8 plotted versus C_2H_6 . There is a weak correlation at JPL. The high XC_2H_6 values
306 exceeding 2.0 ppb were measured in day 314 of 2015 when JPL was downwind of the Aliso Canyon NG leak.
307 Appendix C shows a HYSPLIT back-trajectory confirming this assertion. This spike can also be seen in Fig. 3.
308 There is no C_3H_8 enhancement associated with the C_2H_6 spike, since processed NG was leaking from an
309 underground storage facility, the heavy hydrocarbons (e.g. C_3H_8 , C_4H_{10}) having already been stripped out. A 2%
310 increase in column-averaged CH_4 was also noted in the plume of the Aliso Canyon leak, as shown in Appendix C.

311 California accounts for less than 1% of total U.S. natural gas production and this has declined over the past three
312 decades (<https://www.eia.gov/state/analysis.php?sid=CA>). Although there is natural gas extraction in the LA basin,
313 this is a small source compared with the Permian basin. The local natural gas is only 3% C_2H_6 and 0.3% C_3H_8 ,
314 (<https://www.socalgas.com/stay-safe/pipeline-and-storage-safety/playa-del-rey-storage-operations>) and so cannot
315 account for the approximately equal amounts of these gases measured at JPL by the MkIV. We speculate that the
316 C_3H_8 measured at JPL comes mainly from LPG (e.g. used in "clean" commercial vehicles, BBQ grills, external
317 heaters, etc.). We can certainly rule out the possibility that the C_3H_8 measured at JPL is the result of wild fires, since
318 these have increased in recent years whereas the C_3H_8 has decreased.



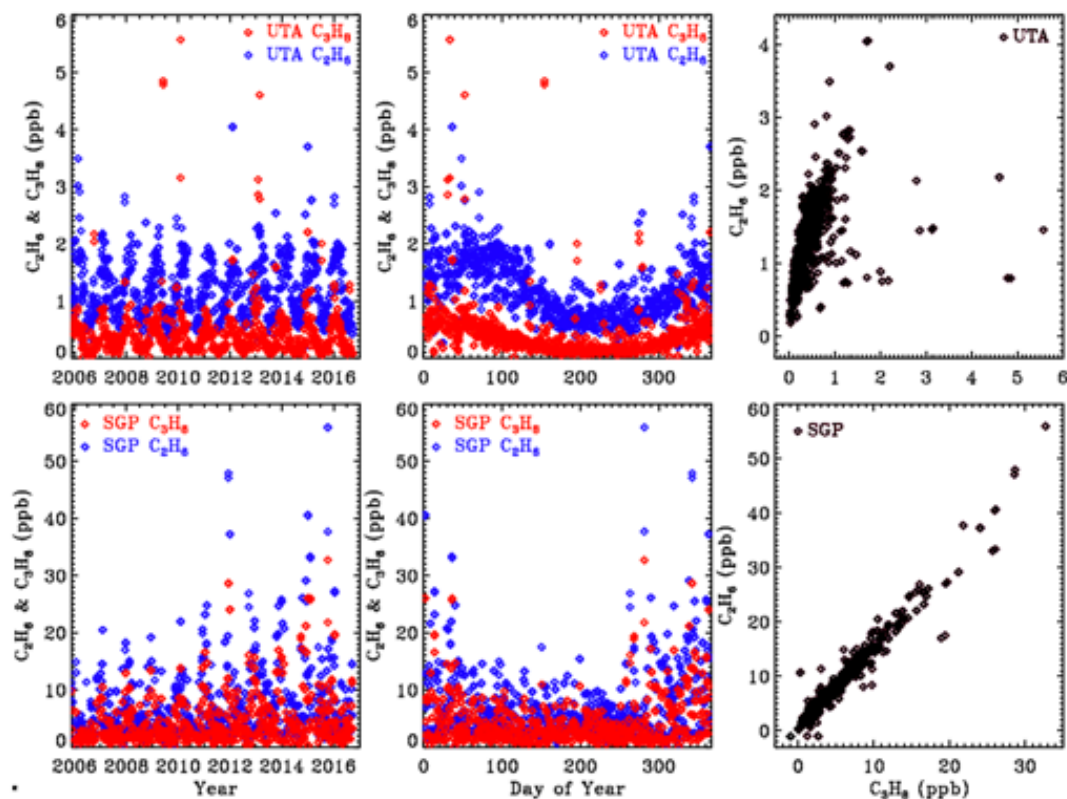
319 3.3. Comparison with In Situ Measurements

320 First a caveat: the column-average mole fractions that are derived from the column measurements will under-
321 estimate the gas amount in the PBL for gases like C_2H_6 and C_3H_8 that reside mainly in the PBL. For example, if
322 C_3H_8 resides entirely between 1000 and 800 mbar, with none in the free troposphere or stratosphere, then the
323 column-average values will be 5 times smaller than the actual mole fractions in the PBL. So direct comparisons of
324 the remote and in situ mole fractions should be avoided. But their behavior as a function of year or season, or gas-to-
325 gas correlations, can still be meaningfully compared. This effect is in addition to the effect of their averaging kernels
326 being less than 1.0 at the surface, which was discussed earlier.

327 In situ C_3H_8 and C_2H_6 mole fractions from the Wendover, Utah (UTA) and Southern Great Plains, Oklahoma (SGP)
328 sites were downloaded from the NOAA Global Monitoring Laboratory website:

329 (<https://www.esrl.noaa.gov/gmd/dv/data/>). These sites are the closest to Ft. Sumner. These are surface flask
330 measurements covering the period 2006 to 2017. Figure 11 illustrates these data as a function of the year (left
331 panels), the day of the year (middle panels), and the C_3H_8 – C_2H_6 relationship (right panels). The upper panels cover
332 the UTA site and the lower panels the SGP site. Note the factor 10 change in the y-scale: there is 10x more of these
333 gases at SGP than at UTA. Looking at the map in Fig.9, this is clearly because SGP lies immediately downwind of
334 the Anadarko Basin oil and NG fields under the prevailing WSW winds. In contrast, the UTA site has no major up-
335 wind source.

336 These in situ measurements confirm that C_3H_8 is highly variable with large enhancements being associated with oil
337 and NG production fields. At SGP the C_3H_8/C_2H_6 ratio is about 0.65. This is smaller than those measured by the
338 MkIV, but NG in the Permian basin is much wetter (richer in C_3H_8) than in the Anadarko basin.



339
340 **Figure 11.** In situ flask measurements of C_3H_8 (red) and C_2H_6 (blue) from the NOAA ESRL GMD dataset (Helmig
341 et al., 2017). Top panels show results from the UTA site and lower panels from SGP. Note the factor 10 change in
342 the y-scale between the two sites. Left panels plot data versus year to illustrate secular trends. Middle panels versus
343 Day of year to more clearly see the seasonal cycle. Right panels plot C_3H_8 versus C_2H_6 .
344

345 3.4. Balloon Results

346 We also attempted to retrieve C_3H_8 from MkIV balloon solar occultation spectra. It was not detected in any flight,
347 despite a very good sensitivity of 0.05 ppb above 5 km. This confirms that the C_3H_8 detected in ground-based
348 measurements, reaching column average mole fractions of up to 4 ppb, resides mostly in the PBL. The balloon
349 launches are typically performed only under stable, quiescent, meteorological conditions with light surface winds.
350 Such conditions preclude uplift of air from the PBL into the free troposphere, so that C_3H_8 stays confined to the
351 PBL, which is opaque in limb paths due to aerosol, and so cannot be probed in occultation. This does not preclude
352 C_3H_8 getting up into the free troposphere at other times or in other places.

353



354 4. Summary and Conclusions

355 We report measurements of atmospheric C₃H₈ by solar absorption spectrometry in the strong Q-branch region at
356 2957 cm⁻¹, using high resolution IR spectra from the JPL MkIV interferometer. To the best of our knowledge, these
357 are the first remote sensing measurements of atmospheric C₃H₈. The minimum detectable abundance is about 10¹⁶
358 molecules.cm⁻², which is roughly equivalent to a column average mole fraction of 0.5 ppb. This allows C₃H₈ to be
359 measured in locations where its abundance is enhanced by proximity to sources (e.g., large gas fields, mega-cities),
360 but not in clean locations (e.g. above the PBL or away from sources). Future improvements to the spectroscopy of
361 the interfering gases, e.g. H₂O, CH₄, C₂H₆, might provide for the detection of C₃H₈ from clean sites at background
362 levels, allow it to become a routine produce of the NDACC and TCCON networks.

363 A case study of ground-based MkIV measurements from Ft. Sumner, New Mexico, show a increasing C₃H₈ and
364 C₂H₆ amounts in the past decade on days when back-trajectories from SE New Mexico and West Texas, where the
365 Permian Basin oil and gas field is located. A case study of C₃H₈ measured at JPL shows a long-term decrease since
366 1990 by more than a factor 2. It also shows a strong correlation with CO, a tracer of urban pollution. There is no
367 significant correlation between C₃H₈ and C₂H₆ at JPL.

368 The MKIV measurements in the case studies are not particularly useful for determining the long-term global trends
369 in C₃H₈ or C₂H₆, due to their close proximity to strong sources. In the case of the Ft. Sumner the source is the
370 Permian Basin. In the case of JPL the source is the Los Angeles urban area with a population of ~15M. These
371 sources cause large meteorology-driven fluctuations that mask the longer-term trends.

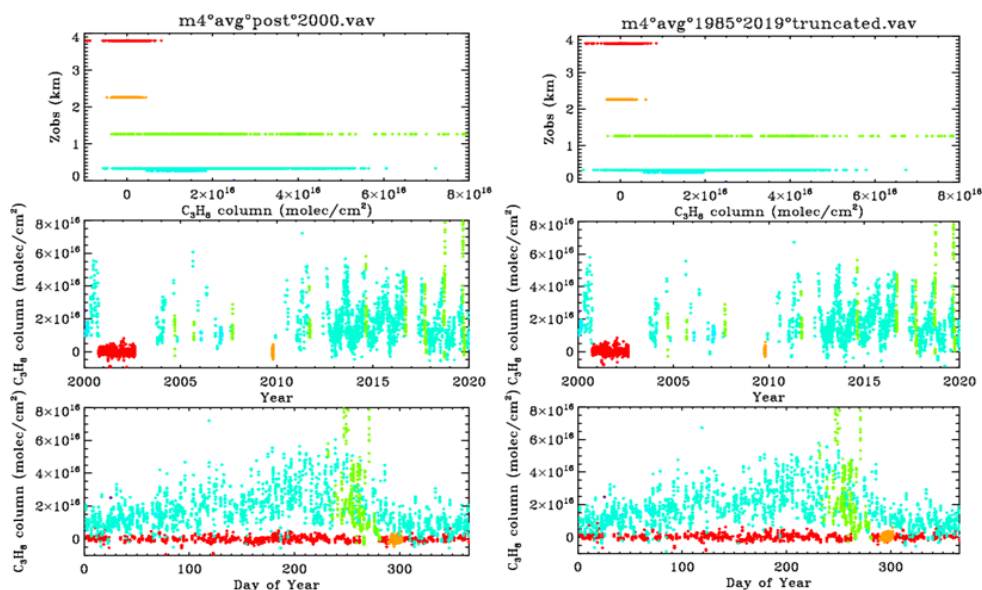
372 From balloon measurements in solar occultation, propane was analyzed using the same window as for the ground-
373 based measurements. It was not detected at any altitude in any of our 25 flights, despite a 0.05 ppb detection limit.
374 This is presumably because under the stable atmospheric conditions that allow balloon launches, C₃H₈ stays
375 confined to the PBL, which is opaque in the limb viewing geometry and so cannot be probed.

376 Appendix A: Sensitivity of retrieved C₃H₈ columns to assumed P, T, and H₂O profiles.

377

378 The retrievals shown in the main body of the paper were performed using 6-hourly NCEP analyses of T, P, and H₂O,
379 exactly as used in the GGG2014 TCCON analyses (Wunch et al., 2006). Due to the overlap of strong H₂O and CH₄
380 lines with the C₃H₈ Q-branch, we were concerned that small errors in the assumed T/P/H₂O/CH₄ priors might
381 strongly influence the retrieved C₃H₈. We therefore re-retrieved C₃H₈ over the 2000–2020 period using the GEOS-
382 FP-IT 3-hourly analyses, which forms the basis of the latest (GGG2020) TCCON analysis (Laughner et al., 2020).
383 We would have done the entire analysis with the GEOS-FP-IT model, except that it only supports the post-2000
384 time period.

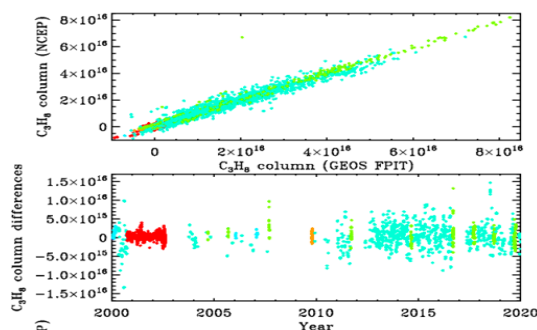
385 Figure A.1 compares the retrieved C₃H₈ columns from the two analysis methods: NCEP in the left panels and
386 GEOS-FP-IT in the right-hand panels. The results look very similar.



387

388 **Figure A.1.** Retrieved vertical columns of C_3H_8 from 2000 to 2020. **Left:** Vertical columns of C_3H_8 retrieved using
 389 the NCEP a priori T/P/ H_2O . **Right:** Vertical columns of C_3H_8 retrieved using the GEOS-FP-IT a priori T/P/ H_2O .

390 Figure A.2 examines more closely the C_3H_8 columns from the two analyses. In the upper panel the NCEP and
 391 GEOS-FPIT columns are plotted against each other. The gradient is 1.011 ± 0.003 with NCEP producing slightly
 392 larger columns. The Pearson correlation coefficient is $+0.979$. The column differences, shown in the lower panel,
 393 are mostly less than $0.5E+16$ and are centered around zero at all column amounts. So the choice of models and
 394 priors makes surprisingly little difference to the retrieved C_3H_8 . This does not mean that the C_3H_8 is highly accurate.
 395 There are many things that are identical between the two analysis (e.g., spectroscopy, retrieval code, spectra) which
 396 could nevertheless contribute large errors to the retrieved C_3H_8 .



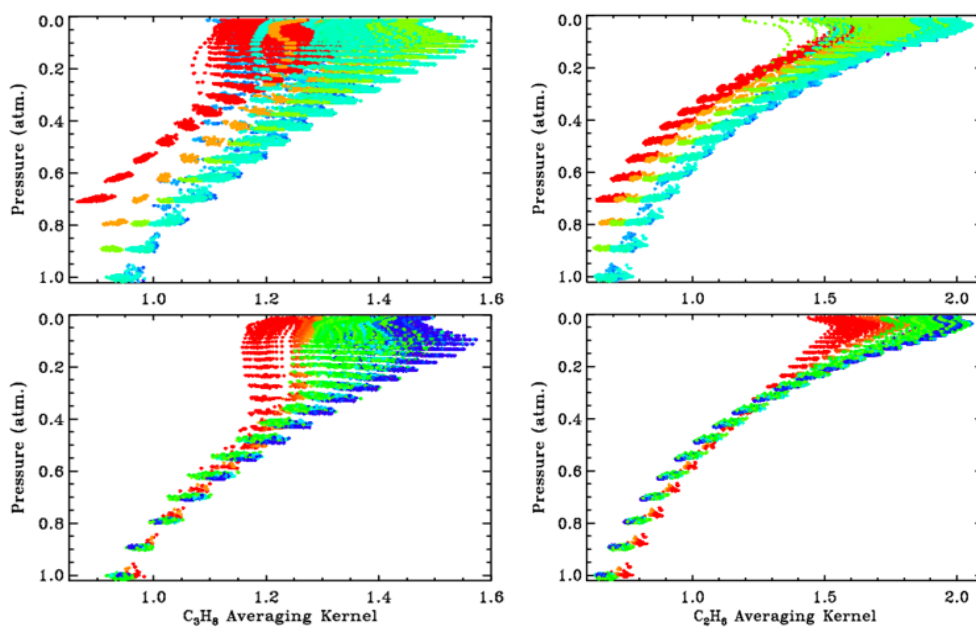
397

398 **Figure A.2.** Comparing the C_3H_8 columns retrieved from the NCEP and GEOS-FPIT priors, color-coded by site
 399 altitude. In the upper panel the columns are plotted against each other. In the lower panel their difference is plotted.



400 **Appendix B: C₃H₈ and C₂H₆ Averaging kernels**

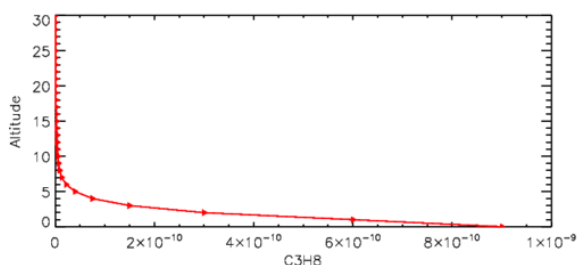
401 Figure B.1 shows all kernels for the 5000 measurements presented in this paper, color-coded by site altitude
402 (red=3.8 km; orange=2.2 km; lime=1.2 km; cyan=0.35 km; blue < 0.2 km) as in the main body of the paper. The
403 kernels increase with altitude but with <40% variation over the 0-30 km altitude range. Note that the kernels
404 representing the 3.8 km site begin at P=0.7 atm. And the kernels representing the 2.2 km site begin at P=0.8 atm.



405

406 **Figure B.1:** 5000 averaging kernels for **Left:** C₃H₈ and **Right:** C₂H₆. Upper panel shows all kernels color-coded by
407 site altitude. Lower panel shows kernels for the low-altitude sites (0.25 to 0.50 km), which were colored blue in the
408 upper panel, now color-coded by solar zenith angle (Blue=15°; Green=60°; Red=80°).

409 The lower panel shows the kernels for the low altitude sites (mainly JPL). These points were all cyan in the upper
410 panel but here they are color-coded by Solar Zenith Angle. It is evident that the higher the SZA the more uniform
411 the kernels with altitude. The banding of the points in pressure space reflects the 1 km vertical grid on which the
412 kernels were computed. The C₃H₈ kernels are also influenced by the H₂O column and temperature, but this is a
413 smaller effect than those of site altitude or SZA.



414

415 **Figure B.2.** *A priori* C_3H_8 profile used in these retrievals.

416 Figure B.2 show the assumed a priori vmr profile, assumed in the retrievals and in the computation of the kernels.
417 Since GFIT performs profile scaling retrievals, the absolute values of the a priori vmr profile play no role, only the
418 shape matters.

419 **Appendix C: - Aliso Canyon Underground Storage Facility: Gas Leak in late 2015**

420 Aliso Canyon Underground Storage Facility is located 30 km NW of JPL. According to the Jan 4, 2016,
421 Los Angeles Times, NG leak began Oct 23, 2015 and peaked on Nov 28 at 60 Tons of CH_4 per hour. By Dec 22 leak
422 rate had decreased to 30 Tons per hour as the underground storage pressure dropped from the initial 2700 psi.

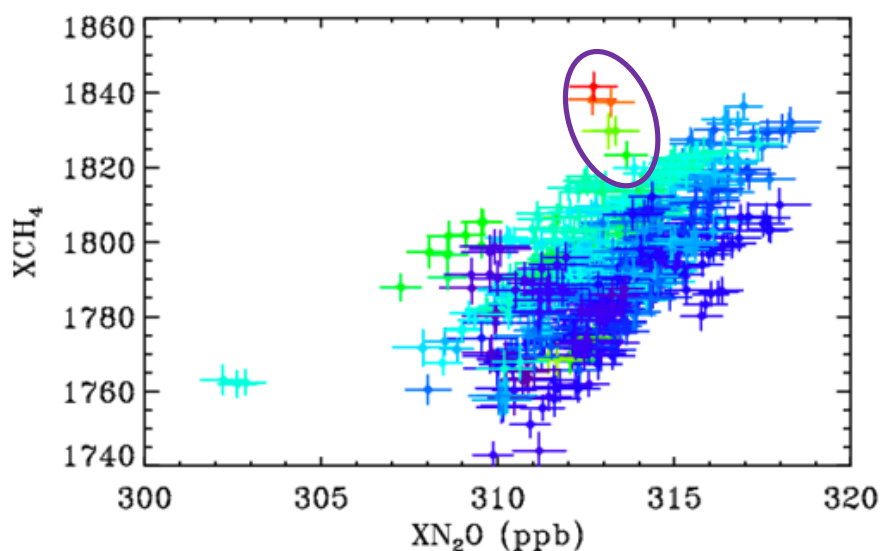


423

424 **Figure C.1.** HYSPLIT back-trajectories for Nov 10, 2015 (day 314) when the highest ever C_2H_6 was measured from
425 JPL. Yellow oval (upper-left) indicates location of Aliso Canyon Underground Storage Facility. Green ball (lower-
426 right) denotes JPL, at the convergence of trajectories arriving at 19, 20, & 21 UT. Trajectory calculation used the
427 NAM 12 km resolution, hybrid sigma-pressure meteorology. © OpenStreetMap contributors 2020. Distributed under a
428 Creative Commons BY-SA License.



429 Large C_2H_6 amounts (3x normal) were observed from JPL on Nov 10 (Day 314), but no enhancement of C_3H_8 .
430 HYSPLIT back-trajectories for this day indicate that the air arriving at JPL at 1000m above ground was from the
431 North-West and had passed over Aliso Canyon USF, confirming that the air over JPL was contaminated by the leak.



432

433 **Figure C.2.** Showing the relationship between CH_4 and N_2O at JPL in 2014–2017 color-coded by C_2H_6 . Blue points
434 represent low C_2H_6 whereas red represents the highest C_2H_6 . The encircled points represent Nov. 10, 2015, whose
435 back-trajectory is shown in previous figure.

436 Most of the variation in column CH_4 and N_2O is associated with the stratospheric circulation. Old airmasses from
437 high latitude are depleted in CH_4 and N_2O . To remove these effects, and be able to more clearly see changes driven
438 by the troposphere, XCH_4 is plotted versus XN_2O which is similarly affected by stratospheric circulation, but not by
439 tropospheric emissions. This creates a correlation with the lower-left points representing high-latitude stratospheric
440 airmasses and the upper right low-latitude airmasses.

441 The encircled points on Fig. C.2 were measured on Nov 10, 2015, when JPL was downwind of the Aliso Canyon
442 USF leak. The indicate XCH_4 enhancements of over 2%, which probably represent a 10+% enhancement in the
443 PBL with no enhancement above. There is also a general tendency for higher CH_4 values when C_2H_6 is elevated on
444 other days too, as seen from the dark blue points (low C_2H_6) being predominantly in the lower right of the figure and
445 the greener points (higher C_2H_6) being located toward the upper left.

446 Code Availability

447 The GFIT code used for the analysis of MkIV spectra is identical to that used by the TCCON project. It is publicly
448 available under license from the California Institute of Technology for non-commercial use. It can be cloned from:



449 hg clone <https://parkfalls.gps.caltech.edu/tcon/stable/hg/ggg-stable/>
450 after signing the license agreement and being issued a password.

451

452 **Data Availability**

453 The ground-based MKIV data used in this paper can be downloaded from two sites:

454 <https://mark4sun.jpl.nasa.gov/ground.html>

455 <ftp://ftp.cpc.ncep.noaa.gov/ndacc/station/barcroft/ames/fiir/>

456 **Authors Contributions**

457 Toon, Sung, Blavier for data acquisition. Toon and Yu for data interpretation.

458 **Competing Interests**

459 No competing interests.

460 **Acknowledgements**

461 The authors gratefully acknowledge the NOAA Air Resources Laboratory (ARL) for the provision of the HYSPLIT
462 transport and dispersion model and/or READY website (<https://www.ready.noaa.gov>) used in this publication. We
463 also acknowledge the NOAA ESRL GMD for distributing in situ data of C₃H₈ and C₂H₆. We thank NASAs Upper
464 Atmosphere Composition Observation (UACO) program for funding support.

465 **References**

- 466 Angelbratt, J. et al. Carbon monoxide (CO) and ethane (C₂H₆) trends from ground-based solar FTIR measurements
467 at six European stations, comparison and sensitivity analysis with the EMEP model. *Atmos. Chem. Phys.* **11**,
468 9253–9269 (2011)
- 469 Conley, S., G. Franco, I. Faloona, D. R. Blake, J. Peischl, T. B. Ryerson, Methane emissions from the 2015 Aliso
470 Canyon blowout in Los Angeles, *Science* (2016), 351, (6279), 1317–1320
- 471 Dalsøren, S.B., Myhre, G., Hodnebrog, Ø. et al. Discrepancy between simulated and observed ethane and propane
472 levels explained by underestimated fossil emissions, *Nature Geoscience*, **11**, 178–184 (2018).
473 <https://doi.org/10.1038/s41561-018-0073-0>
- 474 Franco, B. et al. Retrieval of ethane from ground-based FTIR solar spectra using improved spectroscopy: recent
475 burden increase above Jungfrauoch. *J. Quant. Spec. Radiat. Trans.* **160**, 36–49 (2015).
- 476 Franco, B. et al. Evaluating ethane and methane emissions associated with the development of oil and natural gas
477 extraction in North America. *Environ. Res. Lett.* **11**, 044010 (2016).
- 478 Harrison, JJ and Bernath, PF 2010, Infrared absorption cross sections for propane (C₃H₈) in the 3 μm region, *Journal*
479 *of Quantitative Spectroscopy and Radiative Transfer*, 111, 1282–1288, DOI: 10.1016/j.jqsrt.2009.11.027
- 480 Helmig, D., Rossabi, S., Hueber, J. et al. Reversal of global atmospheric ethane and propane trends largely due to
481 US oil and natural gas production. *Nature Geosci* **9**, 490–495 (2016). <https://doi.org/10.1038/ngeo2721>



- 482 Helmig, D. et al. Climatology and atmospheric chemistry of the non-methane hydrocarbons ethane and propane over
483 the North Atlantic. *Elementa* 3 (2015).
- 484 Helmig D., Hueber J., Tans P. (2017), Non-Methane Hydrocarbons from the NOAA ESRL Surface Network, 2004–
485 2016.
- 486 Irion, F. W., Gunson, M. R., Toon, G. C., Chang, A. Y., Eldering, A., Mahieu, E., Manney, G. L., Michelsen, H. A.,
487 Moyer, E. J., Newchurch, M. J., Osterman, G. B., Rinsland, C. P., Salawitch, R. J., Sen, B., Yung, Y. L., and
488 Zander, R.: Atmospheric Trace Molecule Spectroscopy (ATMOS) Experiment Version 3 data retrievals, *Appl.*
489 *Opt.*, 41, 6968–6979, 2002
- 490 Rolph, G., Stein, A., and Stunder, B., (2017). Real-time Environmental Applications and Display sYstem: READY.
491 *Environmental Modelling & Software*, **95**, 210–228
- 492 Rosado-Reyes, C. M., and J. S. Francisco (2007), Atmospheric oxidation pathways of propane and its by-products:
493 Acetone, acetaldehyde, and propionaldehyde, *J. Geophys. Res.*, 112, D14310, doi:10.1029/2006JD007566.
- 494 Stein, A.F., Draxler, R.R., Rolph, G.D., Stunder, B.J.B., Cohen, M.D., and Ngan, F., (2015). NOAA's HYSPLIT
495 atmospheric transport and dispersion modeling system, *Bull. Amer. Meteor. Soc.*, **96**, 2059-2077
- 496 Sung, K., G. Toon, A. W. Mantz, and M. A. H. Smith (2013), FTIR measurements of cold C₃H₈ cross sections at 7–
497 15 um for Titan atmosphere, *Icarus*, 226, 1499–1513, doi:10.1016/j.icarus.2013.07.028
- 498 Toon, G.C., The JPL MkIV Interferometer, *Opt. Photonics News*, 2, 19–21, 1991
- 499 Toon, G. C., Blavier, J.-F., Sung, K., Rothman, L. S., and Gordon, I., HITRAN spectroscopy evaluation using solar
500 occultation FTIR spectra, *J. Quant. Spectrosc. Ra.*, 182, 324–336, <https://doi.org/10.1016/j.jqsrt.2016.05.021>,
501 2016.
- 502 Toon, G. C., Blavier, J.-F. L., and Sung, K.: Atmospheric carbonyl sulfide (OCS) measured remotely by FTIR solar
503 absorption spectrometry, *Atmos. Chem. Phys.*, 18, 1923–1944, <https://doi.org/10.5194/acp-18-1923-2018>,
504 2018a.
- 505 Toon, G. C., Blavier, J.-F. L., and Sung, K.: Measurements of atmospheric ethene by solar absorption FTIR
506 spectrometry, *Atmos. Chem. Phys.*, 18, 5075–5088, <https://doi.org/10.5194/acp-18-5075-2018>, 2018b.
- 507 Wunch, D., Toon, G. C., Blavier, J.-F. L., Washenfelder, R. A., Notholt, J., Connor, B. J., Griffith, D. W. T.,
508 Sherlock, V., and Wennberg, P. O.: The total carbon column observing network, *Philos. T. R. Soc. A*, 369,
509 2087–2112, <https://doi.org/10.1098/rsta.2010.0240>, 2011.
- 510 Touché Howard, Thomas W. Ferrara & Amy Townsend-Small (2015) Sensor transition failure in the high flow
511 sampler: Implications for methane emission inventories of natural gas infrastructure, *Journal of the Air & Waste*
512 *Management Association*, 65:7, 856-862, DOI: 10.1080/10962247.2015.1025925
- 513 The NEED Project. (2017). Propane [pdf]. Retrieved from
514 <http://www.need.org/files/curriculum/infobook/propane.pdf>
- 515 Urbanski, Shawn P., Wei Min Hao and Stephen Baker, Chemical Composition of Wildland Fire Emissions, Chapter
516 4, *Developments in Environmental Science*, Volume 8, 79–107, A. Bytnerowicz, M. Arbaugh, A. Riebau and C.
517 Andersen (Editors), ISSN: 1474-8177/DOI:10.1016/S1474-8177(08)00004-1